

Oblique crushing of truncated conical sandwich shell with corrugated core

Mao Yang, Bin Han, Pengbo Su, Feihao Li, Zhongnan Zhao, Qi Zhang, Qiancheng Zhang, Zhenjun Hong & Tian Jian Lu

To cite this article: Mao Yang, Bin Han, Pengbo Su, Feihao Li, Zhongnan Zhao, Qi Zhang, Qiancheng Zhang, Zhenjun Hong & Tian Jian Lu (2020): Oblique crushing of truncated conical sandwich shell with corrugated core, *Mechanics of Advanced Materials and Structures*, DOI: [10.1080/15376494.2020.1743396](https://doi.org/10.1080/15376494.2020.1743396)

To link to this article: <https://doi.org/10.1080/15376494.2020.1743396>



Published online: 31 Mar 2020.



Submit your article to this journal [↗](#)



Article views: 15




View related articles [↗](#)



View Crossmark data [↗](#)

Oblique crushing of truncated conical sandwich shell with corrugated core

Mao Yang^{a,b,c} , Bin Han^{b,d}, Pengbo Su^{a,c}, Feihao Li^{a,c}, Zhongnan Zhao^{a,c}, Qi Zhang^b, Qiancheng Zhang^a, Zhenjun Hong^{e,f}, and Tian Jian Lu^{c,g}

^aState Key Laboratory for Strength and Vibration of Mechanical Structures, Xi'an Jiaotong University, Xi'an, China; ^bSchool of Mechanical Engineering, Xi'an Jiaotong University, Xi'an, China; ^cState Key Laboratory of Mechanics and Control of Mechanical Structures, Nanjing University of Aeronautics and Astronautics, Nanjing, China; ^dResearch Institute of Xi'an Jiaotong University, Zhejiang, Hangzhou, China; ^eInstitute of Technology, Inner Mongolia First Machinery Group Corporation, Baotou, China; ^fMaterial Science and Engineering Institute, Shanghai Jiao Tong University, Shanghai, China; ^gNanjing Center for Multifunctional Lightweight Materials and Structures, Nanjing University of Aeronautics and Astronautics, Nanjing, China

ABSTRACT

All-metallic truncated conical sandwich shells with corrugated cores (TCSS) were investigated for crashworthiness under quasi-static oblique compression using a combined experimental and numerical approach. Subsequently, multi-objective optimization design of the TCSS was also performed by adopting the algorithm of NSGA-II to achieve maximum specific energy absorption (SEA) and minimum peak force (F_p). Compared with a monolithic shell, the TCSS exhibits much higher SEA and lower F_p under oblique loading, especially with its semi-apical angle set around 10° to 15° . The results provide valuable guidance for the application of truncated conical sandwich tubes in protective engineering, such as vehicle crashworthiness.

ARTICLE HISTORY

Received 20 December 2019
Accepted 12 March 2020

KEYWORDS

Corrugated core; energy absorption; multi-objective optimization; oblique crushing; truncated conical sandwich shells

1. Introduction

With the development of automotive industry, especially electric vehicles. It is even more important to find a new ultra-light and efficient energy-absorbing structure [1]. The metal thin-walled structures have been widely used in crashworthiness applications, such as automotive industry for their excellent energy absorption capacity, lightweight and convenient preparation. Thin-walled metal tubes, e.g. cylindrical tubes [2–4], square tubes [5, 6], triangular tubes [7], multi-corner tubes [8, 9], multi-cell tubes [10–12], foam filled tubes [13, 14] and hierarchical tubes [15, 16] have high levels of crashworthiness attributed to their lightweight and efficient energy absorption. Existing studies of these thin-walled tubular structures have focused mainly on their crushing behavior and energy absorption under axial loading [17]. During actual collision events, however, the thin-walled structures used as energy absorbers were seldom crushed by pure axial impacting, but rather subjected to a combination of axial and oblique crushing loads. Even the safety standard for vehicle design demands that the frontal protection system (i.e. bumper) should be designed to endure an oblique load, with the loading angle up to 30° [18]. Therefore, it is of great significance to explore the oblique crushing behaviors of thin-walled tubular structures.

For square tubes under oblique compressive loading, global bending was identified as the dominant deformation mechanism underlying energy absorption [19, 20]. For

circular tubes under oblique loading, both the peak force (F_p) and specific energy absorption (SEA) decreased as the loading angle was increased [21]. Han et al. [22] investigated the crushing behavior of square columns subjected to oblique loading, and explored the critical loading angle at which a transition occurred from the axial collapse mode to the bending collapse mode. The axial and oblique crushing behaviors of multi-cell straight tubes with different cross-sectional shapes were numerically simulated [23]: circular cross-section was identified as the best morphology for energy absorption. For a thin-walled straight tube under oblique loading, its overall instability with bending collapse is prone to occur [24], resulting in much lower energy absorption efficiency, compared to the case under axial loading.

In contrast to the thin-walled straight tube, a tapered thin-walled tube usually possesses higher SEA, as bending failure rarely occurs under oblique loading [25, 26]. Moreover, the tapered thin-walled tube exhibits more stable force–displacement curve and lower F_p under oblique or axial loading [25, 27]. By comparing the oblique crushing behaviors of various multi-cell square tubes, it was revealed that a multi-cell tapered tube exhibited the best energy absorption performance in terms of both SEA and peak crushing force (PCF) [28].

In addition to thin-walled tubes, there have been many studies on sandwich structures with periodic cellular cores such as pyramid lattice or corrugated cores, and it has been

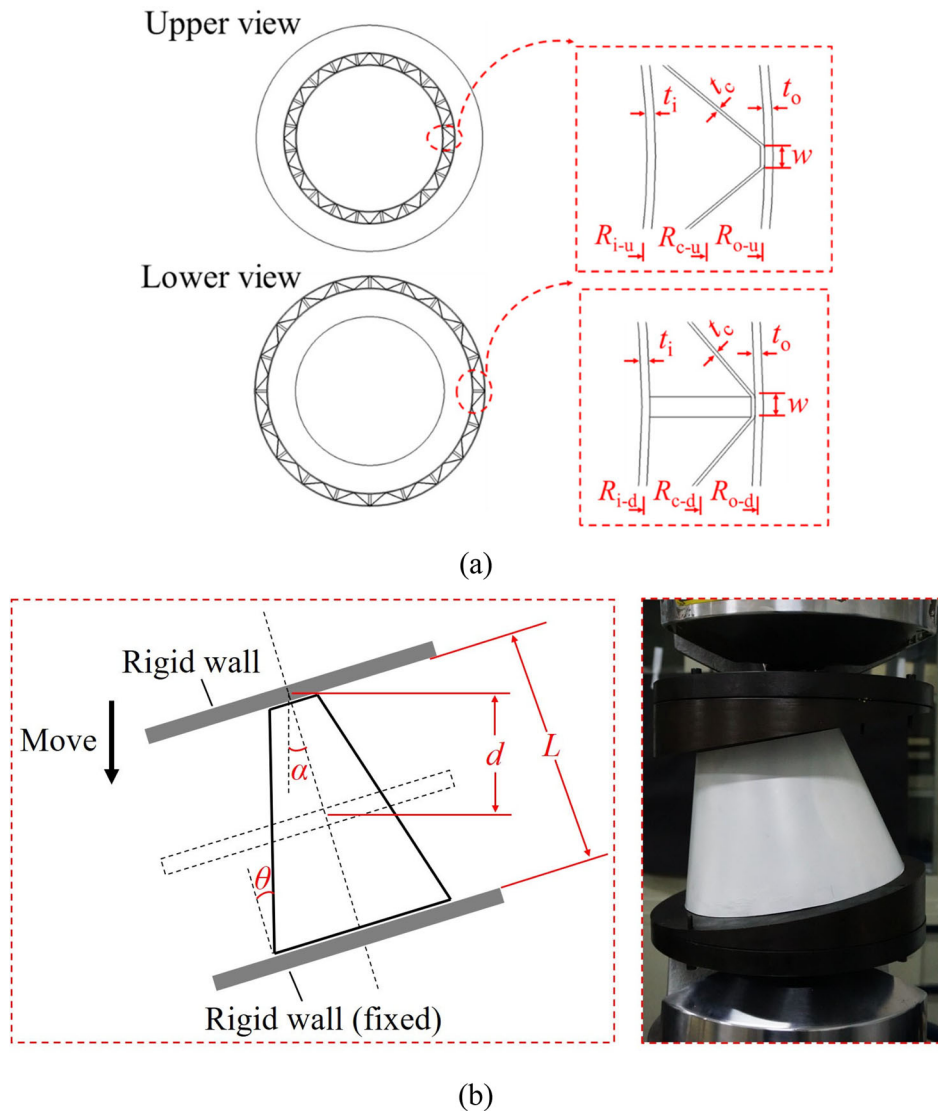


Figure 1. Geometric parameters of TCSS. (a) The geometric dimensions of the upper and lower sections of the TCSS, including wall thickness and radius, etc. The left side of (b) is a schematic diagram of oblique compression testing, the height L and the semi-apical angle θ of the TCSS are given, and the loading angle α and the loading displacement d are defined. The right side of (b) is the corresponding experimental test chart.

found that it has excellent properties, such as ultra-light-weight, superior specific energy absorption, as well as multifunctional attributes [29–33]. While existing research focused mostly upon sandwich plates and beams. There are only a few studies on the energy absorption of sandwich cylindrical shells. Liu et al. [34–36] studied the energy absorption characteristics of sandwich cylindrical shells, and found that the sandwich structure is an excellent energy absorption structure because of its unique coupling effect. However, the core of the structure in their study only contacted the inner and outer panels without physical connection. Besides, few studies on the energy absorption characteristics of sandwich conical shells. Our recent work [37, 38] demonstrated great advantage of cylindrical or truncated conical sandwich shells when subjected to axial compression, relative to their monolithic counterparts. However, there is yet a report concerning the oblique crushing behavior of truncated conical sandwich shells.

In the current study, oblique crushing of all-metallic truncated conical sandwich shells with corrugated cores (TCSS) was systematically investigated under quasi-static oblique compression. A combined experimental study and numerical simulation with the method of finite elements (FE) was carried out. Parametric study based on FE simulations was subsequently carried out to quantify the effects of semi-apical angle and panel thickness. Finally, response surface models (RSM) for F_p and SEA of the TCSS were established for under varying loading angle, and multi-objective optimal design of the TCSS was obtained using the genetic algorithm of NSGA-II.

2. Experimental procedures

2.1. Fabrication methodology

The two conical face sheets and a conical corrugated core form the TCSS. The fabrication processes was divided into

four steps: (a) preparation of corrugated sheet by stamping, (b) shape correction of the ring-shaped and tapered corrugated core, (c) fabricating the face sheets, and (d)

Table 1. Geometric parameters of TCSS.

	t_o (mm)	t_c (mm)	t_i (mm)	R_{i-u} (mm)	R_{o-u} (mm)	R_{i-d} (mm)	R_{o-d} (mm)	w (mm)	θ ($^\circ$)	L (mm)	N
S-444	0.4	0.4	0.4	57.7	66.7	95.0	104.9	2.0	14.9	145.0	20
S-424	0.4	0.2	0.4	57.7	66.7	95.0	104.9	2.0	14.9	145.0	20

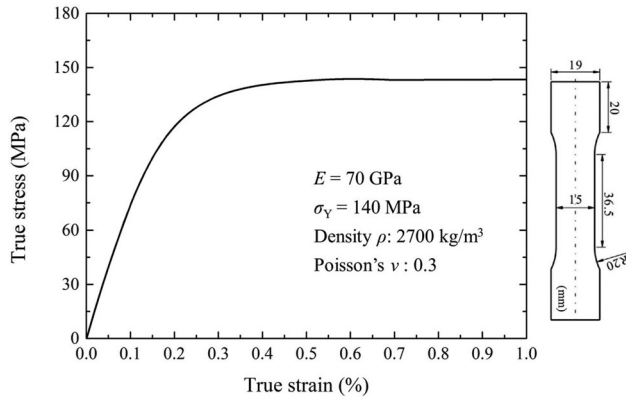


Figure 2. The measured tensile stress versus strain curve for 1060 Al.

assembling; more details were referred to our previous work [38]. Besides, the material of TCSS was 1060Al. Fundamental mechanical properties of 1060Al, Young's modulus and yield stress, were obtained by uniaxial tensile testing [38].

For oblique compression testing, two groups of TCSS specimens with different wall thickness of corrugated core were fabricated. Relevant geometrical parameters of the TCSS structures were presented in Figure 1 and Table 1. Where N is the number of circumferential corrugations. For convenience, specimens with $t_c = 0.4$ mm were named S-444, and specimens with $t_c = 0.2$ mm were named S-424. The loading angle was set to be either $\alpha = 0^\circ$ or $\alpha = 10^\circ$ for the testing.

2.2. Experimental testing

Quasi-static oblique compression tests with a load angle of $\alpha = 10^\circ$ were carried out using a MTS, as shown in Figure 1b. The top platen was moved vertically downwards to compress the specimen. And the speed fixed at 1.0 mm/min, the specimen in each group was compressed by a displacement of 80 mm. During compression testing, load and displacement data were obtained. It should be noted that, during

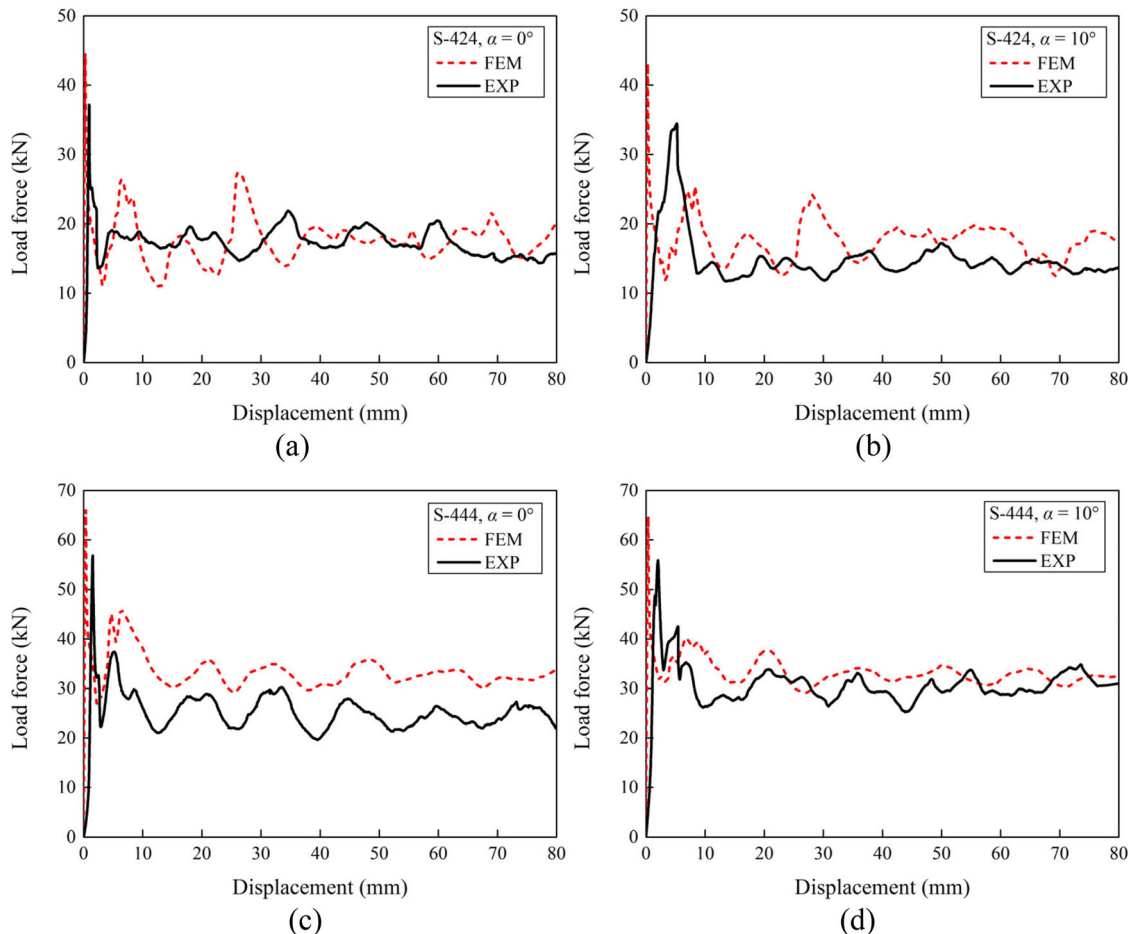
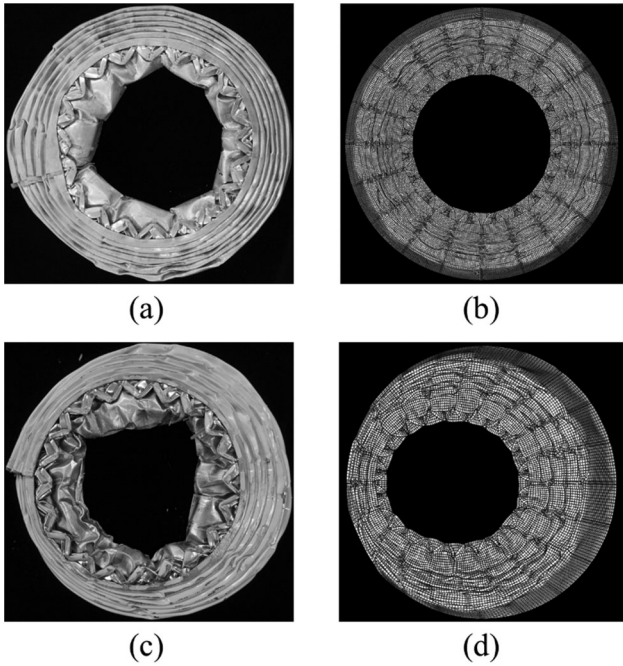


Figure 3. Comparison between experimental and numerical load versus deflection curves for TCSS specimens (Table 2) under axial and oblique loading: (a) S-424a, corresponding loading angle $\alpha = 0^\circ$, (b) S-424b, corresponding loading angle $\alpha = 10^\circ$, (c) S-444a, corresponding loading angle $\alpha = 0^\circ$ and (d) S-444b, corresponding loading angle $\alpha = 10^\circ$.

Table 2. Oblique crushing characteristics of TCSS: comparison between FE simulations and experiments.

Specimen	t_o (mm)	t_c (mm)	t_i (mm)	A (°)	F_p (kN)		SEA (kJ/kg)	
					FEM	EXP	FEM	EXP
S-424a	0.4	0.2	0.4	0	44.55	37.20	6.53	6.38
S-424b				10	43.10	34.45	6.64	5.45
S-444a	0.4	0.4	0.4	0	66.09	56.88	9.98	7.49
S-444b				10	64.77	55.89	9.90	8.69

**Figure 4.** Comparison of final deformed morphology between numerical simulations (FEM) and experiments (EXP) for TCSS specimens under axial and oblique compression: (a) EXP and (b) FEM of S-444a, corresponding loading angle $\alpha = 0^\circ$, (c) EXP and (d) of S-444b, corresponding loading angle $\alpha = 10^\circ$.

compression, the friction force in the contact interface between the TCSS and the top/bottom platens was self-locking, as the oblique load angle was small and there was no slippage between the TCSS and the platens. Due to strong light reflection at the 1060Al surface, it was not conducive to observe the deformation process of TCSS. Thus, a thin layer of paint was sprayed on the surface of TCSS for enhanced visibility, which would not influence the mechanical properties of TCSS [39].

3. Finite element simulation

3.1. Finite element model

The crushing and energy absorption behaviors under oblique loading of the TCSS were analyzed by full three-dimensional finite element (FE) simulations with ABAQUS/Explicit. The geometrical parameters were same as the experimental specimens, whereas the material properties were identical to those reported in [38], listed in Figure 2, and the isotropic hardening model is used and the material constitutive is simulated using the true stress–strain curve as showed in Figure 2. Two rigid plates were employed to

model the top and bottom platens, using four-node rigid elements (R3D4). The TCSS (both corrugated and face sheets) was modeled using 4-node shell elements (S4R) [40]. Upon checking the convergence of the present numerical solutions, the optimal mesh size for TCSS was found to be 2×2 mm. For all the FE simulations, the boundary condition and loading conditions were shown in Figure 1b. In order to be consistent with the experiment, in Section 3.2, the TCSS is in contact with the top and bottom rigid plates. In the following parametric discussion and optimization, the “Tie” connection is set between the TCSS and rigid plates. An automatic surface-to-surface contact is defined between the top rigid/bottom rigid plate and the TCSS. An automatic surface-to-surface contact is defined between the face sheets and corrugated core. Besides, an automatic single surface contact is defined to simulate self-contact of corrugated core or face sheet. And Coulomb friction coefficient of 0.2 [38] is employed for all the contacts.

3.2. Comparison between FE simulations and experimental results

For validation, Figure 3 compared the experimentally measured load force–displacement curves with FE results. In addition, Table 2 summarized the F_p and SEA obtained by both simulations and experiments. The final deformed morphology of TCSS from experiments was also compared with that from simulations, as shown in Figure 4. Overall, the experimental results were in good agreement with the simulations. The experimentally measured values of F_p and SEA were nonetheless somewhat lower than those numerically calculated. This may be because some uncontrollable fabrication-induced defects, e.g. small pits or link defects, which would cause premature buckling of the specimen.

4. Parametric study

4.1. Effect of the semi-apical angle

As previously discussed for cases under axial compression [38], the semi-apical angle was one of the critical parameters dictating the failure modes and energy absorption performance. In this subsection, the influence of θ on the oblique crushing performance of TCSS was discussed based on FE simulation results. The total mass of the TCSS structures simulated equaled to that of specimen S-424, the thickness ratio was fixed at $t_f/t_c = 2$, and the compression distance was fixed at 80 mm. Figure 5 presented the load versus displacement curves of TCSSs with different θ (0° – 20°) under varying loading angle α (0° – 30°). The force versus displacement curve exhibited large reciprocating fluctuations for the case with small α , induced by the continuous formation of plastic hinges [38]. As α was increased, the fluctuation gradually disappeared and the curve became relatively smooth, since global instability occurred at sufficiently large α , as implied from the deformation modes shown in Figure 6. The results of Figure 6 suggested further that the TCSS with a higher θ had a stronger ability to resist overall instability.

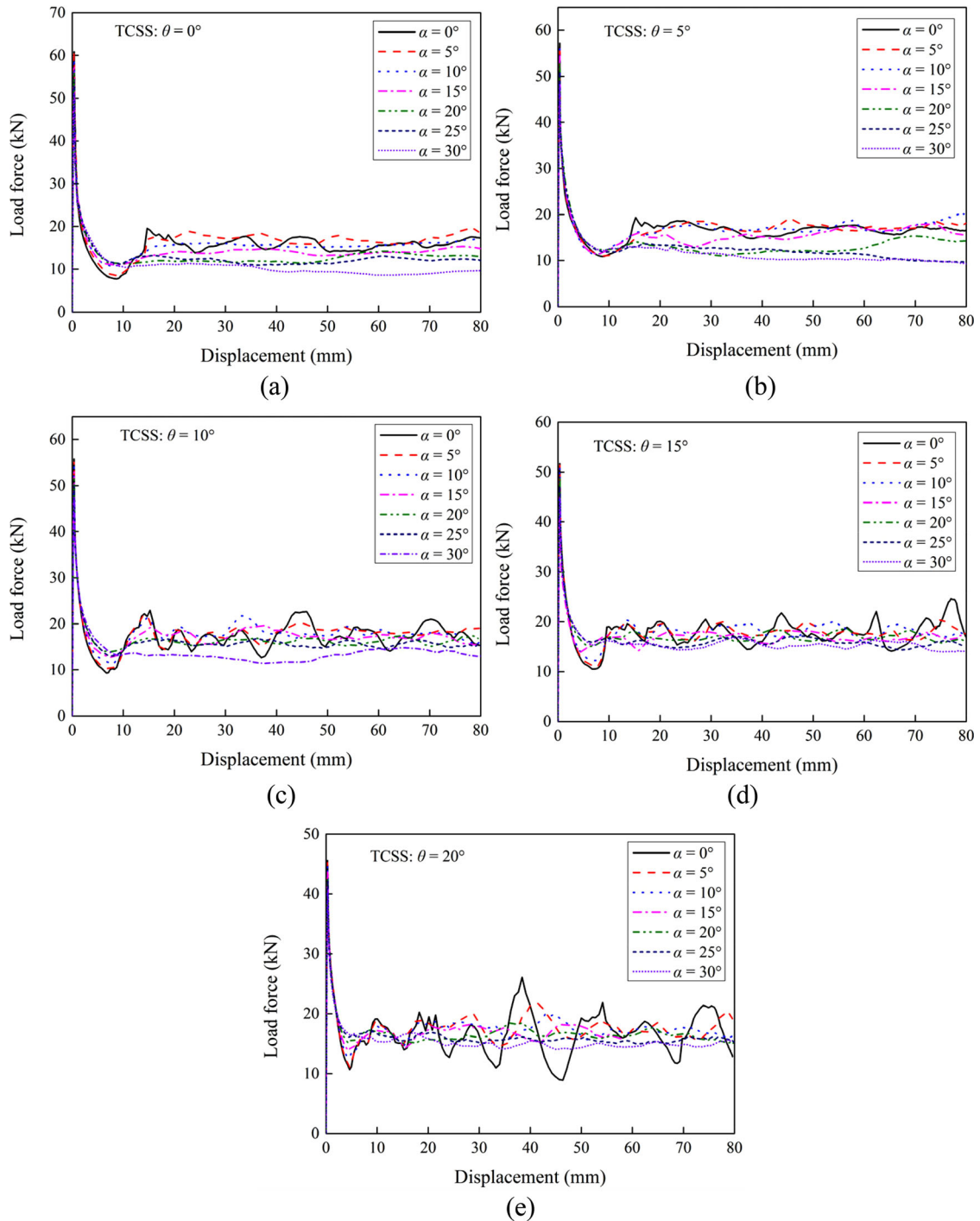


Figure 5. Load versus displacement curves of TCSS under varying load angle ($\alpha = 0^\circ/5^\circ/10^\circ/15^\circ/20^\circ/25^\circ/30^\circ$): (a) Semi-apical angle $\theta = 0^\circ$, (b) Semi-apical angle $\theta = 5^\circ$, (c) Semi-apical angle $\theta = 10^\circ$, (d) Semi-apical angle $\theta = 15^\circ$ and (e) Semi-apical angle $\theta = 20^\circ$. All structures have equal mass, the thickness ratio was fixed at $t_f/t_c = 2$.

Figure 7 presented the simulated effects of θ and α on SEA and F_p . Overall, for the cases with a constant α , as θ was increased, the SEA increased firstly, peaking at $\theta = 10^\circ - 15^\circ$, and then decreased. In particular, the TCSS with $\theta = 10^\circ$ exhibited overall instability at large loading angles. Therefore, as α was increased, the SEA for the TCSS with $\theta = 10^\circ$ became gradually lower than the TCSS with $\theta = 20^\circ$. (More detailed description of the critical loading angle was given immediately below.) Besides, the F_p of TCSS monotonically decreased with increasing θ because, as

θ was increased, the bending moment induced by the load force increased, resulting in the structure more prone to instability. For cases with constant θ , the SEA increased firstly and then decreased as the loading angle α was increased. In contrast, the F_p decreased with increasing α because the shear force induced by compressive force increased correspondingly, making the structure more susceptible to instability.

It could be seen from Figures 6 and 7(a) that, for each TCSS, three regions emerged from the relationship between

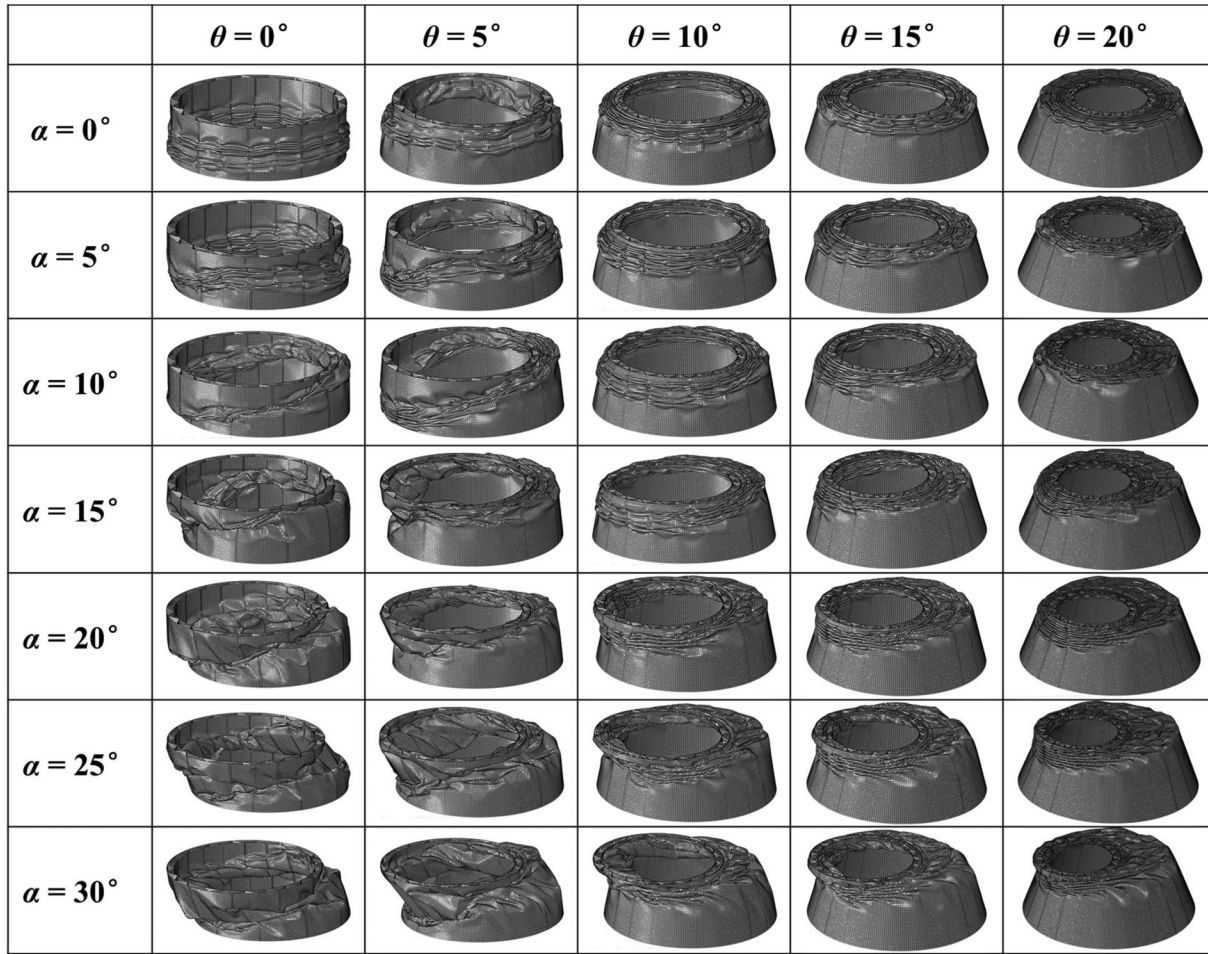


Figure 6. Effects of semi-apical angle θ and loading angle α on numerically simulated deformation modes of TCSS. All structures have equal mass, the thickness ratio was fixed at $t_i/t_c = 2$.

SEA and α : Region ① where progressive collapse dominated (progressive region), Region ② where there was a transition from progressive to global bending collapse (transition region), and Region ③ where global bending collapse dominated the global structure. Further examination of the results displayed in Figures 6 and 7(a) revealed that the critical loading angle α_{tr} for the transition mode (i.e. Region ②) lied within the range of 7° – 8° for the case of $\theta = 0^\circ$, 16° – 17° for the case of $\theta = 5^\circ$, and 28° – 29° for the case of $\theta = 10^\circ$. Nevertheless, the TCSSs with θ of 15° or 20° collapsed entirely by progressive crushing under oblique loading (loading angle ranging from 0° to 30°). This further demonstrated that the TCSS under oblique loading had a better ability to resist global instability as θ was increased. In addition, the energy absorption behaviors (SEA and F_p) of the TCSS were compared with monolithic conical shells (MCS) having equivalent mass, θ and maximum outer diameter, as illustrated in Figure 8. The results showed that the TCSS had a higher SEA and a lower F_p than the MCS. Under the oblique loading, the interaction effect between the face panels and the core prohibits the TCSS from global buckling and promotes the formation of stable plastic hinges, leading to much better crashworthiness performance than the MCS.

4.2. Effect of face sheet thickness

Figure 9 presented the effects of face sheet thickness t ($t = t_o = t_i = t_c$) on SEA and F_p of TCSS with $\theta = 15^\circ$ for selected loading angles. For TCSSs with different θ , the influence of face sheet thickness on energy absorption exhibited nearly the same trend, as detailed in Appendix A. The results of Figure 9 demonstrated that the SEA increased with increasing t , since the bending stiffness of TCSS increased correspondingly and hence overall instability was less likely to happen. However, it was not conducive that the F_p of TCSS increased monotonically with the increase of t , undesirable for energy absorbers. Therefore, it is necessary to conduct multi-objective optimization to achieve high SEA but low F_p , as demonstrated in the section to follow.

5. Optimal design

5.1. Response surface models

With the development of computer technology, some engineering problems have been well solved based on computer optimization technology [41–48]. In order to achieve optimized response of a TCSS under oblique loading, the

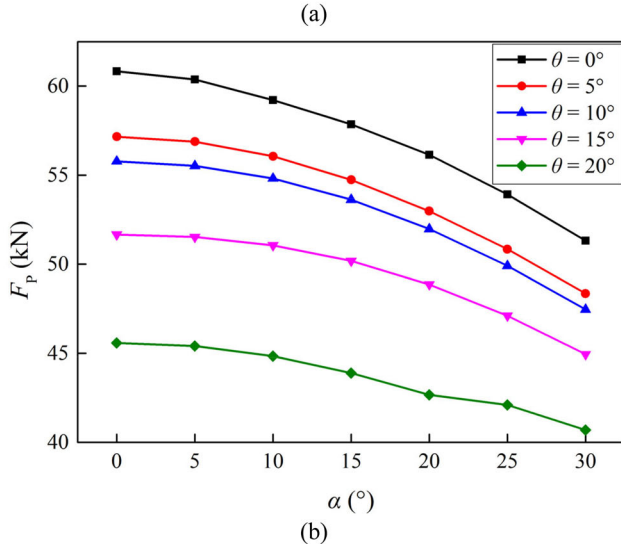
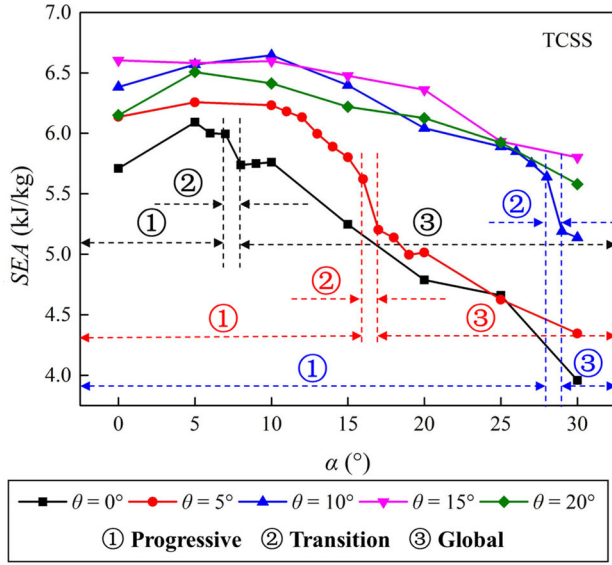


Figure 7. Effects of semi-apical angle θ and loading angle α on (a) SEA and (b) F_p . All structures have equal mass, the thickness ratio was fixed at $t_t/t_c = 2$. (a) Divides the SEA of the structure with α into three regions (① Progressive, ② Transition and ③ Global), represents the deformation modes of the structures. The angle corresponding to region ② is the critical loading angle.

surrogate model approach, e.g. response surface model (RSM), was applied which has been proven particularly effective [49–51]. The RSM was considered as an efficient approximation method in the optimal design problems involving complex nonlinear mechanics such as contact and large plastic deformation. The basic idea of RSM was to express a complex function $f(x)$ in terms of a series of simple basis function $\varphi_i(x)$. The mathematical equations of RSM was written as

$$f(x) \approx f(\tilde{x}) = \sum_{i=1}^m \delta_i \varphi_i(x) \quad (1)$$

where $f(x)$ and $f(\tilde{x})$ were the response surface approximation and the numerical solution denoting for $f(x)$, respectively. m represents the total number of basic functions $\varphi_i(x)$, and δ_i was the unknown coefficient. A typical class of basic functions was the polynomials whose full linear form was given as

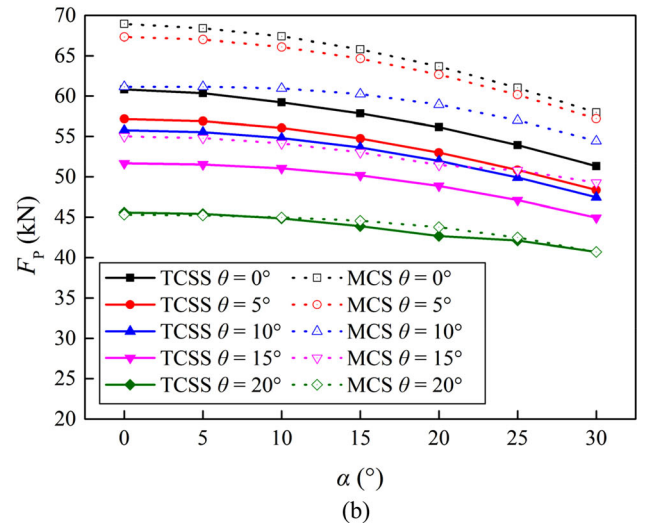
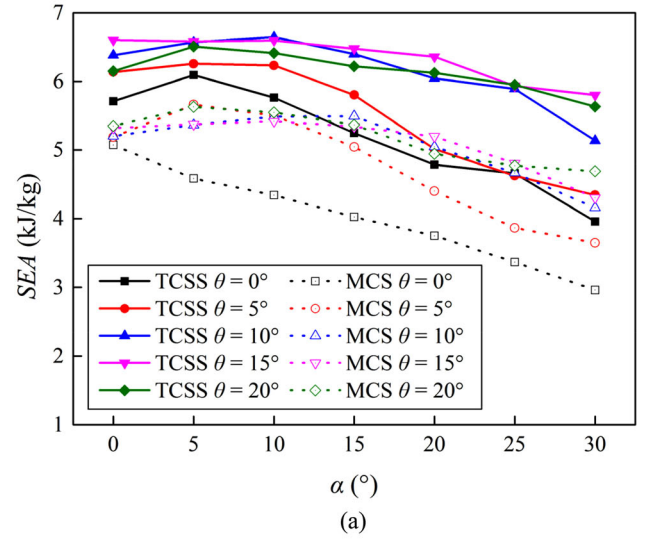


Figure 8. Comparison of energy absorption behaviors of TCSS and MCS subjected to oblique compressive loading: (a) SEA and (b) F_p . All TCSSs have equal mass, the thickness ratio was fixed at $t_t/t_c = 2$. And the monolithic conical shells (MCS) have equivalent mass and same maximum outer diameter as TCSS.

$$1, x_1, x_2, \dots, x_n \quad (2)$$

And full cubic polynomial was given as

$$1, x_1, x_2, \dots, x_n, x_1^2, x_1 x_2, \dots, x_1 x_n, \dots, x_n^2, x_1^3, x_1^2 x_2, \dots, x_1^2 x_n, x_1 x_2^2, \dots, x_1 x_n^2, \dots, x_n^3 \quad (3)$$

In this section, based on the, design of experiments (DOEs), the RSM for predicting both the SEA and F_p with respect to design variables t and θ were constructed for four representative loading angles (0° , 10° , 20° , 30°), as summarized in Table 3. The upper and lower limits of t were set to be 1.0 mm and 0.2 mm, and the upper and lower limits of θ were 20° and 0° . The other geometrical dimensions were same as those of experimental specimens were listed in Table 1.

The multiple regression fitting method was used to fit numerical results which were listed in Table 3. Then, mathematical equations of RSM for both the SEA and F_p were obtained, which showed in Appendix B.

The accuracy of RSM is verified by some indicators, e.g. the R square values (R^2), the adjusted square error (R^2_{adj}) and the P -value were evaluated using normalized expressions, as:

$$R^2 = 1 - SSE/SST, \quad SST = \sum_{i=1}^N (y_i - \bar{y}_i)^2 \quad (4)$$

$$R^2_{adj} = 1 - (1 - R^2) \frac{N - 1}{N - p - 1}$$

where y_i and \bar{y}_i denoted the FE solution and the mean value of the FE results, respectively; SSE and SST were the sum of square errors and the total sum of squares; p was the number of non-constant terms in the RSM.

Value of R^2 , R^2_{adj} and P were listed in Table 4. All the values of R^2 and R^2_{adj} were more than 0.98, and all the values of P were 0. So, the present RSM showed sufficient accuracy.

To view the effect of both t and θ synthetically, the RSM for SEA and F_p prediction was depicted in Figure 10. As t was increased, the value of SEA increased, but the growth rate decreased. As θ was increased, the value of SEA increased firstly, peaking at $\theta = 10^\circ - 15^\circ$, then decreased after θ was further increased. Besides, as t or θ was increased, F_p increased.

5.2. Multi-objective optimal design

Based upon the constructed RSM, the algorithm of NSGA-II [52] was applied to find the Pareto designs. The Pareto optimal designs of the maximum SEA and minimum F_p were presented in Figure 11. To verify the accuracy, full three-dimensional FE simulations of TCSS were carried out based upon the ‘‘Knee point.’’ Table 5 compared the FE results with the optimized results. The errors between FE results and optimization solutions for both the SEA and F_p were less than 4%.

6. Conclusions

The crashworthiness characteristics of TCSS under oblique loading were investigated using a combined experimental and numerical approach. Parametric study based on finite element simulations was carried out to quantify the influence of semi-apical angle θ and face sheet thickness t on

Table 3. Sample points and relevant numerical results on these points.

No.	t (mm)	θ ($^\circ$)	$\alpha = 0^\circ$		$\alpha = 10^\circ$		$\alpha = 20^\circ$		$\alpha = 30^\circ$	
			SEA (kJ/kg)	F_p (kN)	SEA (kJ/kg)	F_p (kN)	SEA (kJ/kg)	F_p (kN)	SEA (kJ/kg)	F_p (kN)
1	0.2	0	5.15	29.64	5.30	28.28	4.16	26.32	4.16	24.44
2	0.2	2.5	4.88	29.94	5.41	29.15	4.60	27.05	3.94	24.75
3	0.2	5	6.45	28.53	6.45	27.88	6.11	26.34	4.78	24.12
4	0.2	7.5	6.62	28.57	6.75	27.93	6.61	26.27	4.70	24.00
5	0.2	10	6.86	27.17	6.86	26.66	6.58	25.25	6.26	23.39
6	0.2	15	6.94	22.99	6.86	22.60	6.78	21.31	6.28	19.68
7	0.2	20	7.18	16.27	7.04	15.91	5.64	14.86	5.68	12.97
8	0.4	0	8.17	90.78	8.24	89.14	7.56	83.74	6.94	76.10
9	0.4	2.5	8.35	89.06	8.73	87.40	7.91	82.30	7.09	74.57
10	0.4	5	8.79	85.61	9.01	84.07	8.77	79.21	7.13	71.77
11	0.4	7.5	9.19	82.22	9.58	80.69	9.28	76.16	8.67	68.98
12	0.4	10	8.95	77.57	9.58	76.29	9.12	72.22	8.77	65.46
13	0.4	15	10.32	64.72	10.16	63.43	9.56	59.53	8.77	55.16
14	0.4	20	10.31	44.07	9.81	43.50	9.18	40.06	8.56	36.45
15	0.6	0	10.32	155.58	10.48	152.51	9.60	142.67	8.59	130.09
16	0.6	2.5	10.58	151.37	11.05	148.41	11.07	140.19	8.67	127.94
17	0.6	5	11.30	140.88	11.20	139.44	10.96	133.08	10.12	122.34
18	0.6	7.5	12.20	134.10	11.82	132.87	11.30	128.00	10.43	117.70
19	0.6	10	11.78	126.19	11.99	124.22	11.39	119.12	10.65	111.05
20	0.6	15	12.49	107.08	12.50	105.19	11.70	100.55	10.84	92.90
21	0.6	20	11.63	80.02	11.79	76.26	11.04	72.41	10.26	66.56
22	0.8	0	12.10	217.96	12.12	213.47	10.99	200.99	9.81	183.24
23	0.8	2.5	13.70	210.21	13.53	206.59	12.83	195.77	10.00	178.90
24	0.8	5	13.60	198.10	13.36	194.29	12.90	185.87	11.75	171.54
25	0.8	7.5	13.90	188.60	14.01	185.12	13.20	176.59	12.11	163.89
26	0.8	10	14.45	175.93	14.11	173.78	13.27	166.63	12.09	154.34
27	0.8	15	14.17	149.43	14.17	147.55	13.38	141.15	12.28	130.45
28	0.8	20	13.83	114.11	13.05	112.22	12.75	106.72	11.37	98.78
29	1.0	0	13.63	281.06	13.98	273.92	12.23	258.68	10.74	235.78
30	1.0	2.5	14.17	268.57	14.52	264.13	13.94	250.02	11.13	229.82
31	1.0	5	14.77	255.33	14.52	250.95	13.97	238.68	12.61	219.83
32	1.0	7.5	15.00	241.23	15.17	237.71	14.47	227.20	13.11	209.22
33	1.0	10	15.45	224.62	14.96	221.54	14.38	212.65	13.25	197.41
34	1.0	15	15.71	191.95	15.11	189.05	14.41	180.58	13.26	167.86
35	1.0	20	14.61	156.54	14.71	145.45	13.76	138.15	12.66	127.88

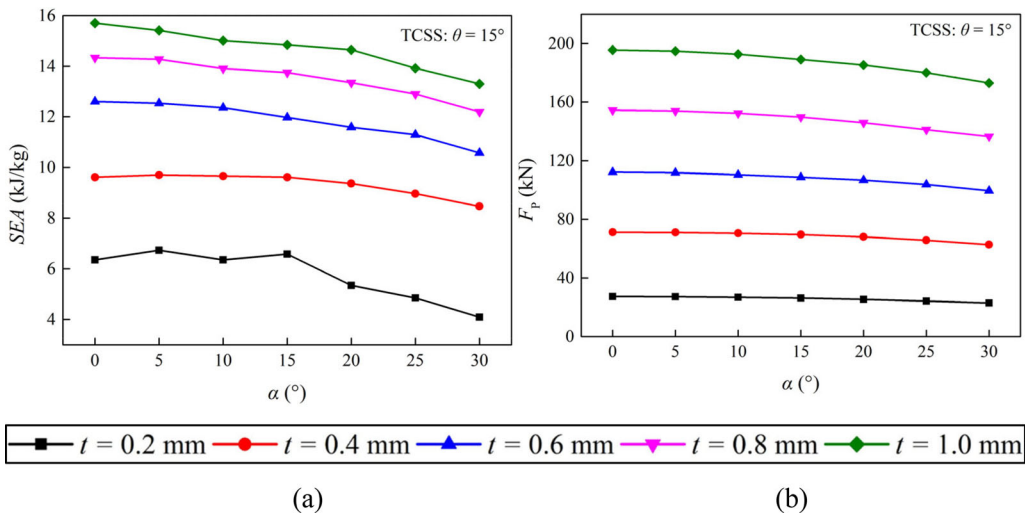


Figure 9. Effects of face sheet thickness t and loading angle α on SEA and F_p , where, semi-apical angle of TCSS is 15° .

Table 4. Accuracy evaluation of the RSM.

	$\alpha = 0^\circ$		$\alpha = 10^\circ$		$\alpha = 20^\circ$		$\alpha = 30^\circ$	
	SEA	F_p	SEA	F_p	SEA	F_p	SEA	F_p
R^2	0.983	0.999	0.982	0.999	0.980	0.999	0.981	0.999
P	0.000	0.000	0.000	0.000	0.000	0.000	0.000	0.000
R^2_{adj}	0.983	0.999	0.982	0.999	0.980	0.999	0.981	0.999

SEA and F_p of the TCSS. The critical load angle and the corresponding deformation mechanism were also discussed. Response surface model (RSM) for SEA and F_p of the TCSS under oblique loading with different load angles α was established by the multivariate regression method. Multi-objective optimization design (MOD) of the TCSS was

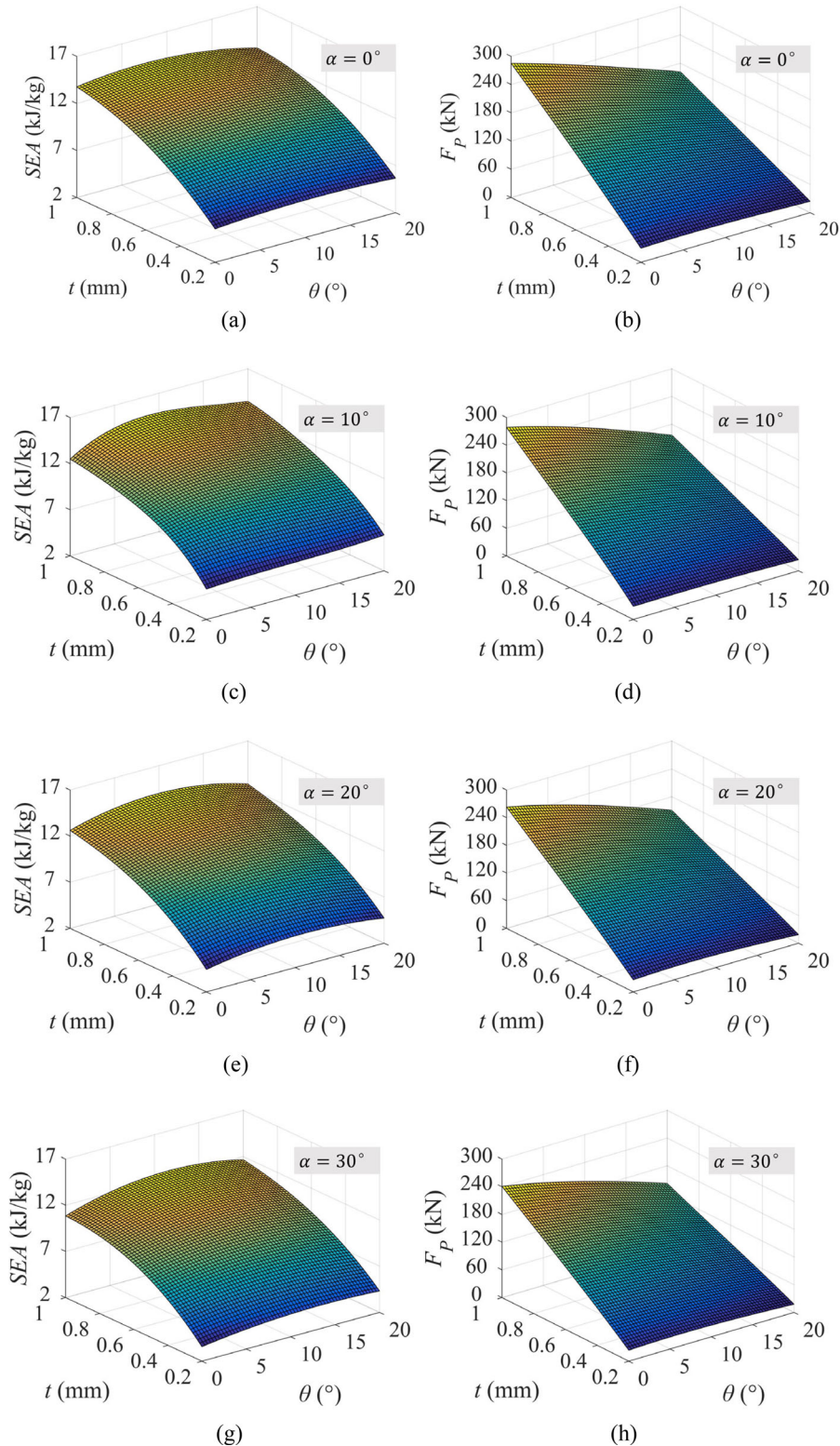


Figure 10. RSM of SEA and F_p for TCSS under different load angles: (a) SEA and (b) F_p for loading angle $\alpha = 0^\circ$, (c) SEA and (d) F_p for loading angle $\alpha = 10^\circ$, (e) SEA and (f) F_p for loading angle $\alpha = 20^\circ$, (g) SEA and (h) F_p for loading angle $\alpha = 30^\circ$.

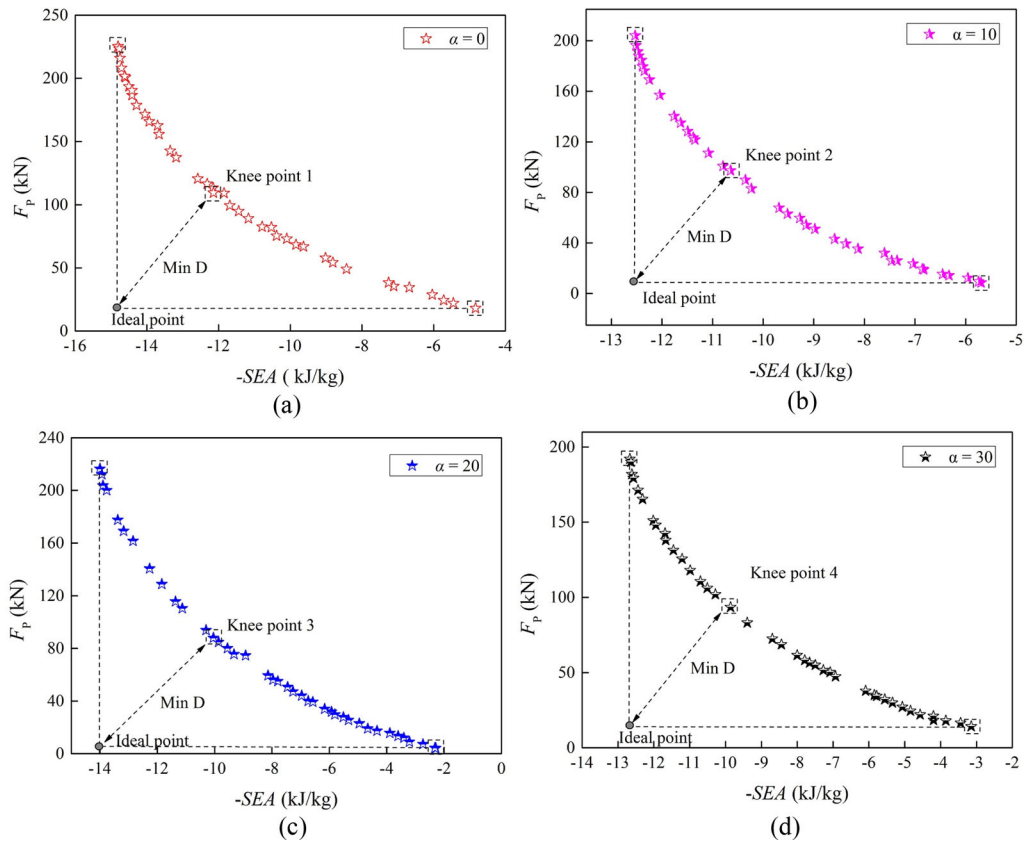


Figure 11. Pareto front for optimal SEA and F_p : (a) $\alpha = 0^\circ$, (b) $\alpha = 10^\circ$, (c) $\alpha = 20^\circ$ and (d) $\alpha = 30^\circ$.

Table 5. Optimum points.

Knee point	t (mm)	θ ($^\circ$)	Mass (g)	SEA (kJ/kg)			F_p (kN)		
				Opt. result	FEM result	Error (%)	Opt. result	FEM results	Error (%)
$\alpha = 0^\circ$	0.69	18.71	451.30	13.12	13.28	1.18	102.68	102.95	0.26
$\alpha = 10^\circ$	0.69	19.50	448.16	12.97	12.50	3.69	100.07	97.74	2.38
$\alpha = 20^\circ$	0.58	18.67	377.73	10.94	11.34	3.66	87.94	89.76	2.03
$\alpha = 30^\circ$	0.63	17.46	413.32	10.86	11.13	2.41	86.78	84.77	2.37

performed with the algorithm of NSGA-II. Main findings were summarized as follows:

- With α fixed and θ increased, the SEA increased firstly, peaking at $\theta = 10^\circ - 15^\circ$, and then decreased. The F_p monotonically decreased with increasing θ . When θ was fixed, the SEA increased firstly and then decreased with increasing α , while F_p decreased. Increasing t led to the increase of both the SEA and F_p .
- When subjected to oblique loading, the TCSS had a better ability to resist global instability as θ was increased. The critical load angle lied within the transition range of $7^\circ-8^\circ$ for the TCSS with $\theta = 0^\circ$, $16^\circ-17^\circ$ for the TCSS with $\theta = 5^\circ$, and $28^\circ-29^\circ$ for the TCSS with $\theta = 10^\circ$. The TCSS with θ of 15° or 20° collapsed entirely via progressive crushing across the full range of load angles ($0^\circ-30^\circ$).
- The Pareto fronts for maximum SEA and minimum F_p under different loading angles were obtained with multi-objective optimization design.

This study has demonstrated that TCSSs are advantageous in energy absorption under oblique loading, which provides valuable guidance for their applications in protective engineering, such as vehicle crashworthiness.

Disclosure statement

No potential conflict of interest was reported by the authors.

Funding

This work was supported by the National Natural Science Foundation of China (11802221, 11972185 and 51875441), the National Key R&D Program of China (2018YFB1106400), the China Postdoctoral Science

Foundation (2016M600782), the Postdoctoral Scientific Research Project of Shaanxi Province (2016BSHYDZZ18), the Zhejiang Provincial Natural Science Foundation of China (LGG18A020001), and the Natural Science Basic Research Plan in Shaanxi Province of China (2018JQ1078) the Open Fund of the State Key Laboratory of Mechanics and Control of Mechanical Structures (MCMS-I-0219K01 and MCMS-E-0219K02), China.

ORCID

Mao Yang  <http://orcid.org/0000-0002-0062-2446>

References

- [1] R.H. Zhang, Z.C. He, H.W. Wang, F. You, and K.N. Li, Study on self-tuning tyre friction control for developing main-servo loop integrated chassis control system, *IEEE Access.*, vol. 5, pp. 6649–6660, 2017. DOI: [10.1109/ACCESS.2017.2669263](https://doi.org/10.1109/ACCESS.2017.2669263).
- [2] R. Shams, A. Niknejad, A.G. Olabi, and M.Z. Nejad, Quasi-static flattening energy absorption process on preformed circular tubes by numerical and experimental analyses, *Thin Wall Struct.*, vol. 144, pp. 106260, 2019. DOI: [10.1016/j.tws.2019.106260](https://doi.org/10.1016/j.tws.2019.106260).
- [3] H. Hatami, M.S. Rad, and A.G. Jahromi, A theoretical analysis of the energy absorption response of expanded metal tubes under impact loads, *Int. J. Impact Eng.*, vol. 109, pp. 224–239, 2017. DOI: [10.1016/j.ijimpeng.2017.06.009](https://doi.org/10.1016/j.ijimpeng.2017.06.009).
- [4] K.A. Praveen, M.N. Mohamed, A. Jusuf, T. Dirgantara, and L. Gunawan, Axial crash performance of press-formed open and end-capped cylindrical tubes – A comparative analysis, *Thin Wall Struct.*, vol. 124, pp. 468–488, 2018. DOI: [10.1016/j.tws.2017.12.037](https://doi.org/10.1016/j.tws.2017.12.037).
- [5] G. Sun, T. Pang, C. Xu, G. Zheng, and J. Song, Energy absorption mechanics for variable thickness thin-walled structures, *Thin Wall Struct.*, vol. 118, pp. 214–228, 2017. DOI: [10.1016/j.tws.2017.04.004](https://doi.org/10.1016/j.tws.2017.04.004).
- [6] S. Ming, C. Zhou, T. Li, Z. Song, and B. Wang, Energy absorption of thin-walled square tubes designed by kirigami approach, *Int. J. Mech. Sci.*, vol. 157–158, pp. 150–164, 2019. DOI: [10.1016/j.ijmecsci.2019.04.032](https://doi.org/10.1016/j.ijmecsci.2019.04.032).
- [7] Z. Fan, G. Lu, T.X. Yu, and K. Liu, Axial crushing of triangular tubes, *Int. J. Appl. Mech.*, vol. 05, no. 01, pp. 1350008, 2013. DOI: [10.1142/S1758825113500087](https://doi.org/10.1142/S1758825113500087).
- [8] A. Malekshahi, K.H. Shirazi, and M. Shishehsaz, Axial crushing of prismatic multi-corner metal columns considering plastic hardening and curvature, *J Mech.*, vol. 35, pp. 1–12, 2018. DOI: [10.1017/jmech.2018.2](https://doi.org/10.1017/jmech.2018.2).
- [9] S. Reddy, M. Abbasi, and M. Fard, Multi-cornered thin-walled sheet metal members for enhanced crashworthiness and occupant protection, *Thin Wall Struct.*, vol. 94, pp. 56–66, 2015. DOI: [10.1016/j.tws.2015.03.029](https://doi.org/10.1016/j.tws.2015.03.029).
- [10] Z. Wang, J. Liu, and S. Yao, On folding mechanics of multi-cell thin-walled square tubes, *Composite B Eng.*, vol. 132, pp. 17–27, 2018. DOI: [10.1016/j.compositesb.2017.07.036](https://doi.org/10.1016/j.compositesb.2017.07.036).
- [11] N. Qiu, Y. Gao, J. Fang, Z. Feng, G. Sun, and Q. Li, Crashworthiness analysis and design of multi-cell hexagonal columns under multiple loading cases, *Finite Elem. Anal. Des.*, vol. 104, pp. 89–101, 2015. DOI: [10.1016/j.finel.2015.06.004](https://doi.org/10.1016/j.finel.2015.06.004).
- [12] Z.C. Li, S. Rakheja, and W.B. Shangguan, Crushing behavior and crashworthiness optimization of multi-cell square tubes under multiple loading angles, *Proc. Inst. Mech. Eng. D J. Automobile Eng.*, vol. 234, no. 05, pp. 1497–1511, 2019. DOI: [10.1177/0954407019869127](https://doi.org/10.1177/0954407019869127).
- [13] F. Xiong, D. Wang, and S. Yin, Optimization analysis of novel foam-filled elliptical columns under multiple oblique impact loading, *Mater. Design.*, vol. 156, pp. 198–214, 2018. DOI: [10.1016/j.matdes.2018.06.057](https://doi.org/10.1016/j.matdes.2018.06.057).
- [14] H. Saeidi Googarchin, M. Pasandidehpour, A. Mahmoodi, and M.H. Shojaeefard, Energy absorption analysis for tapered multi-cell tubes improved by foams: theoretical development and numerical simulation, *Compos. Struct.*, vol. 207, pp. 213–222, 2019. DOI: [10.1016/j.compstruct.2018.09.032](https://doi.org/10.1016/j.compstruct.2018.09.032).
- [15] X. Xu, Y. Zhang, J. Wang, F. Jiang, and C.H. Wang, Crashworthiness design of novel hierarchical hexagonal columns, *Compos. Struct.*, vol. 194, pp. 36–48, 2018. DOI: [10.1016/j.compstruct.2018.03.099](https://doi.org/10.1016/j.compstruct.2018.03.099).
- [16] W. Zhang, S. Yin, T.X. Yu, and J. Xu, Crushing resistance and energy absorption of pomelo peel inspired hierarchical honeycomb, *Int. J. Impact Eng.*, vol. 125, pp. 163–172, 2019. DOI: [10.1016/j.ijimpeng.2018.11.014](https://doi.org/10.1016/j.ijimpeng.2018.11.014).
- [17] A. Pandarkar, M.D. Goel, and M.S. Hora, Axial crushing of hollow and foam filled tubes: an overview, *Sādhanā*, vol. 41, no. 8, pp. 909–921, 2016. DOI: [10.1007/s12046-016-0525-4](https://doi.org/10.1007/s12046-016-0525-4).
- [18] A. Reyes, O.S. Hopperstad, and M. Langseth, Aluminum foam-filled extrusions subjected to oblique loading: experimental and numerical study, *Int J Solids Struct.*, vol. 41, no. 5–6, pp. 1645–1675, 2004. DOI: [10.1016/j.ijsolstr.2003.09.053](https://doi.org/10.1016/j.ijsolstr.2003.09.053).
- [19] A. Reyes, M. Langseth, and O.S. Hopperstad, Square aluminum tubes subjected to oblique loading, *Int. J. Impact Eng.*, vol. 28, no. 10, pp. 1077–1106, 2003. DOI: [10.1016/S0734-743X\(03\)00045-9](https://doi.org/10.1016/S0734-743X(03)00045-9).
- [20] M. Arjomandi Rad and A. Khalkhali, Crashworthiness multi-objective optimization of the thin-walled tubes under probabilistic 3D oblique load, *Mater. Design.*, vol. 156, pp. 538–557, 2018. DOI: [10.1016/j.matdes.2018.07.008](https://doi.org/10.1016/j.matdes.2018.07.008).
- [21] A. Børvik, O.S. Hopperstad, A. Reyes, M. Langseth, G. Solomos, and T. Dyngeland, Empty and foam-filled circular aluminium tubes subjected to axial and oblique quasistatic loading, *Int. J. Crashworthiness.*, vol. 8, no. 5, pp. 481–494, 2003. DOI: [10.1533/ijcr.2003.0254](https://doi.org/10.1533/ijcr.2003.0254).
- [22] D.C. Han and S.H. Park, Collapse behavior of square thin-walled columns subjected to oblique loads, *Thin Wall Struct.*, vol. 35, no. 3, pp. 167–184, 1999. DOI: [10.1016/S0263-8231\(99\)00022-1](https://doi.org/10.1016/S0263-8231(99)00022-1).
- [23] S. Pirmohammad and S.E. Marzdashti, Crushing behavior of new designed multi-cell members subjected to axial and oblique quasi-static loads, *Thin Wall Struct.*, vol. 108, pp. 291–304, 2016. DOI: [10.1016/j.tws.2016.08.023](https://doi.org/10.1016/j.tws.2016.08.023).
- [24] W. Wei and X. Qiu, Analysis of the carrying capacity for tubes under oblique loading, *J. Appl. Mech.*, vol. 85, pp. 031010, 2018. DOI: [10.1115/1.4038921](https://doi.org/10.1115/1.4038921).
- [25] A. Baroutaji, M. Sajjia, and A.G. Olabi, On the crashworthiness performance of thin-walled energy absorbers: recent advances and future developments, *Thin Wall Struct.*, vol. 118, pp. 137–163, 2017. DOI: [10.1016/j.tws.2017.05.018](https://doi.org/10.1016/j.tws.2017.05.018).
- [26] S. Azarakhsh, and A. Ghamarian, Collapse behavior of thin-walled conical tube clamped at both ends subjected to axial and oblique loads, *Thin Wall Struct.*, vol. 112, pp. 1–11, 2017. DOI: [10.1016/j.tws.2016.11.020](https://doi.org/10.1016/j.tws.2016.11.020).
- [27] Y. Zhang, G. Sun, X. Xu, G. Li, and Q. Li, Multiobjective crashworthiness optimization of hollow and conical tubes for multiple load cases, *Thin Wall Struct.*, vol. 82, pp. 331–342, 2014. DOI: [10.1016/j.tws.2014.05.006](https://doi.org/10.1016/j.tws.2014.05.006).
- [28] C. Qi, S. Yang, and F. Dong, Crushing analysis and multiobjective crashworthiness optimization of tapered square tubes under oblique impact loading, *Thin Wall Struct.*, vol. 59, pp. 103–119, 2012. DOI: [10.1016/j.tws.2012.05.008](https://doi.org/10.1016/j.tws.2012.05.008).
- [29] F. Côté, V.S. Deshpande, N.A. Fleck, and A.G. Evans, The compressive and shear responses of corrugated and diamond lattice materials, *Int. J. Solids Struct.*, vol. 43, no. 20, pp. 6220–6242, 2006. DOI: [10.1016/j.ijsolstr.2005.07.045](https://doi.org/10.1016/j.ijsolstr.2005.07.045).

- [30] Y.S. Tian and T.J. Lu, Optimal design of compression corrugated panels, *Thin Wall Struct.*, vol. 43, no. 3, pp. 477–498, 2005. DOI: [10.1016/j.tws.2004.07.014](https://doi.org/10.1016/j.tws.2004.07.014).
- [31] B. Han, K.K. Qin, B. Yu, Q.C. Zhang, C.Q. Chen, and T.J. Lu, Design optimization of foam-reinforced corrugated sandwich beams, *Compos. Struct.*, vol. 130, pp. 51–62, 2015. DOI: [10.1016/j.compstruct.2015.04.022](https://doi.org/10.1016/j.compstruct.2015.04.022).
- [32] B. Han, Z.J. Zhang, Q.C. Zhang, Q. Zhang, and T.J. Lu, Recent advances in hybrid lattice-cored sandwiches for enhanced multifunctional performance, *Extreme Mech. Lett.*, vol. 10, pp. 58–69, 2016. DOI: [10.1016/j.eml.2016.11.009](https://doi.org/10.1016/j.eml.2016.11.009).
- [33] F.H. Roudbeneh, G. Liaghat, H. Sabouri, and H. Hadavinia, Experimental investigation of quasistatic penetration tests on honeycomb sandwich panels filled with polymer foam, *Mech. Adv. Mater. Struct.*, 2018. DOI: [10.1080/15376494.2018.1525628](https://doi.org/10.1080/15376494.2018.1525628).
- [34] W. Liu, Z. Lin, J. He, N. Wang, and X. Deng, Crushing behavior and multi-objective optimization on the crashworthiness of sandwich structure with star-shaped tube in the center, *Thin Wall Struct.*, vol. 108, pp. 205–214, 2016. DOI: [10.1016/j.tws.2016.08.021](https://doi.org/10.1016/j.tws.2016.08.021).
- [35] X. Deng and W. Liu, Experimental and numerical investigation of a novel sandwich sinusoidal lateral corrugated tubular structure under axial compression, *Int. J. Mech. Sci.*, vol. 151, pp. 274–281, 2019. DOI: [10.1016/j.ijmecsci.2018.11.010](https://doi.org/10.1016/j.ijmecsci.2018.11.010).
- [36] X. Deng and W. Liu, Multi-objective optimization of thin-walled sandwich tubes with lateral corrugated tubes in the middle for energy absorption, *Thin Wall Struct.*, vol. 137, pp. 303–317, 2019. DOI: [10.1016/j.tws.2018.12.040](https://doi.org/10.1016/j.tws.2018.12.040).
- [37] P.B. Su, et al., Axial compressive collapse of ultralight corrugated sandwich cylindrical shells, *Mater. Design.*, vol. 160, pp. 325–337, 2018. DOI: [10.1016/j.matdes.2018.09.034](https://doi.org/10.1016/j.matdes.2018.09.034).
- [38] M. Yang, et al., Axial crushing of ultralight all-metallic truncated conical sandwich shells with corrugated cores, *Thin Wall Struct.*, vol. 140, pp. 318–330, 2019. DOI: [10.1016/j.tws.2019.03.048](https://doi.org/10.1016/j.tws.2019.03.048).
- [39] D. Jiang, N. Bechle, C.M. Landis, and S. Kyriakides, Buckling and recovery of NiTi tubes under axial compression, *Int. J. Solids Struct.*, vol. 80, pp. 52–63, 2016. DOI: [10.1016/j.ijsolstr.2015.10.022](https://doi.org/10.1016/j.ijsolstr.2015.10.022).
- [40] T. Belytschko, J.I. Lin, and C.S. Tsay, Explicit algorithms for the nonlinear dynamics of shells, *Comput. Method Appl. Mech. Eng.*, vol. 42, no. 2, pp. 225–251, 1984. DOI: [10.1016/0045-7825\(84\)90026-4](https://doi.org/10.1016/0045-7825(84)90026-4).
- [41] X. Xu, H. Yang, R. Augello, and E. Carrera, Optimized free-form surface modeling of point clouds from laser-based measurement, *Mech. Adv. Mater. Struct.*, 2019. DOI: [10.1080/15376494.2019.1688435](https://doi.org/10.1080/15376494.2019.1688435).
- [42] X. Xu, R. Augello, and H. Yang, The generation and validation of a CUF-based FEA model with laser-based experiments, *Mech. Adv. Mater. Struct.*, pp. 1–8, 2019. DOI: [10.1080/15376494.2019.1697473](https://doi.org/10.1080/15376494.2019.1697473).
- [43] X. Xu, J. Bureick, H. Yang, and I. Neumann, TLS-based composite structure deformation analysis validated with laser tracker, *Compos. Struct.*, vol. 202, pp. 60–65, 2018. DOI: [10.1016/j.compstruct.2017.10.015](https://doi.org/10.1016/j.compstruct.2017.10.015).
- [44] X. Xu, H. Yang, and I. Neumann, A feature extraction method for deformation analysis of large-scale composite structures based on TLS measurement, *Compos. Struct.*, vol. 184, pp. 591–596, 2018. DOI: [10.1016/j.compstruct.2017.09.087](https://doi.org/10.1016/j.compstruct.2017.09.087).
- [45] X. Xu, H. Yang, Y. Zhang, and I. Neumann, Intelligent 3D data extraction method for deformation analysis of composite structures, *Compos. Struct.*, vol. 203, pp. 254–258, 2018. DOI: [10.1016/j.compstruct.2018.07.003](https://doi.org/10.1016/j.compstruct.2018.07.003).
- [46] H. Yang, M. Omidalizari, X. Xu, and I. Neumann, Terrestrial laser scanning technology for deformation monitoring and surface modeling of arch structures, *Compos. Struct.*, vol. 169, pp. 173–179, 2017. DOI: [10.1016/j.compstruct.2016.10.095](https://doi.org/10.1016/j.compstruct.2016.10.095).
- [47] H. Yang, X. Xu, B. Kargoll, and I. Neumann, An automatic and intelligent optimal surface modeling method for composite tunnel structures, *Compos. Struct.*, vol. 208, pp. 702–710, 2019. DOI: [10.1016/j.compstruct.2018.09.082](https://doi.org/10.1016/j.compstruct.2018.09.082).
- [48] H. Yang and X. Xu, Multi-sensor technology for B-spline modelling and deformation analysis of composite structures, *Compos. Struct.*, vol. 224, pp. 111000, 2019. DOI: [10.1016/j.compstruct.2019.111000](https://doi.org/10.1016/j.compstruct.2019.111000).
- [49] G. Sun, G. Li, S. Zhou, H. Li, S. Hou, and Q. Li, Crashworthiness design of vehicle by using multiobjective robust optimization, *Struct. Multidisc. Optim.*, vol. 44, no. 1, pp. 99–110, 2011. DOI: [10.1007/s00158-010-0601-z](https://doi.org/10.1007/s00158-010-0601-z).
- [50] W. Shen, X. Gu, P. Jiang, J. Hu, X. Lv, and L. Qian, Crushing analysis and multiobjective optimization design for rectangular unequal triple-cell tubes subjected to axial loading, *Thin Wall Struct.*, vol. 117, pp. 190–198, 2017. DOI: [10.1016/j.tws.2017.04.018](https://doi.org/10.1016/j.tws.2017.04.018).
- [51] H. Yang, X. Xu, and I. Neumann, Optimal finite element model with response surface methodology for concrete structures based on terrestrial laser scanning technology, *Compos. Struct.*, vol. 183, pp. 2–6, 2018. DOI: [10.1016/j.compstruct.2016.11.012](https://doi.org/10.1016/j.compstruct.2016.11.012).
- [52] K. Deb, A. Pratap, S. Agarwal, and T. Meyarivan, A fast and elitist multiobjective genetic algorithm: NSGA-II, *IEEE Trans. Evol. Comput.*, vol. 6, no. 2, pp. 182–197, 2002. DOI: [10.1109/4235.996017](https://doi.org/10.1109/4235.996017).

Appendix A. Effects of face sheet thickness and loading angle on SEA and F_p

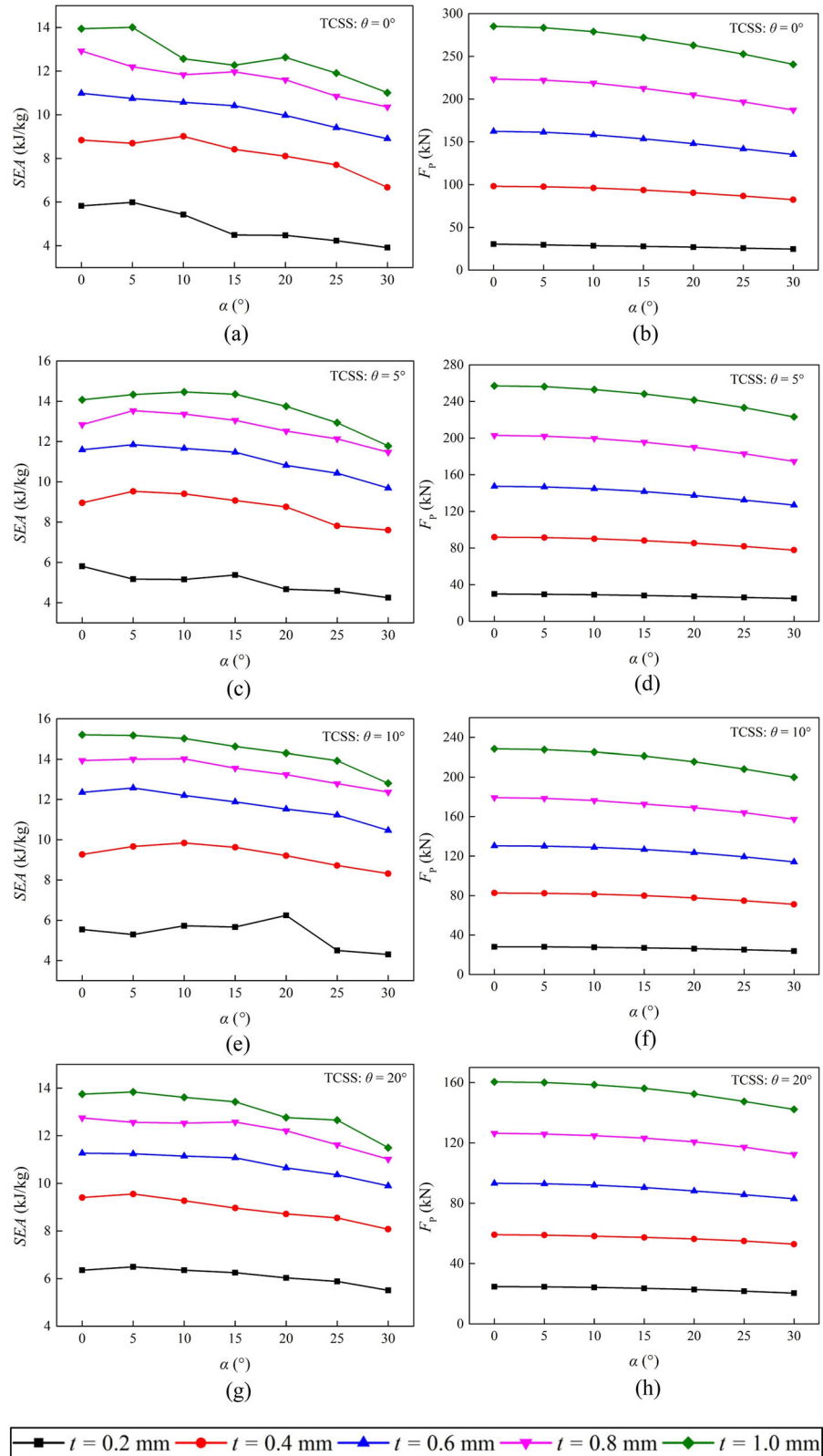


Figure A1. Effects of t and α on SEA and F_p for TCSS structures.

Appendix B. Response surface functions for TCSS structures under oblique compression

For TCSS structures, the fully third-order response surface function for both the SEA and F_p were presented: Eqs. (A.1) and (A.2) were expressions of SEA and F_p for TCSS ($\alpha=0$), (A.3) and (A.4) for TCSS ($\alpha=10$), (A.5) and (A.6) for TCSS ($\alpha=20$), and (A.7) and (A.8) for TCSS ($\alpha=30$).

$$SEA = 1.476 + 22.650t + 0.055\theta - 11.699t^2 - 0.002\theta^2 + 0.119t\theta + 1.327t^3 + 0.031t^2\theta - 0.008t\theta^2 \quad (A.1)$$

$$F_p = -41.421 + 366.430t + 2.232\theta - 53.969t^2 - 0.062\theta^2 - 8.684t\theta + 14.243t^3 + 0.001\theta^3 + 1.097t^2\theta + 0.001t\theta^2 \quad (A.2)$$

$$SEA = -0.328 + 31.830t + 0.213\theta - 26.822t^2 - 0.012\theta^2 - 0.020t\theta + 8.044t^3 + 0.193t^2\theta - 0.009t\theta^2 \quad (A.3)$$

$$F_p = -44.428 + 376.492t + 2.492\theta - 80.685t^2 - 0.078\theta^2 - 8.666t\theta + 27.932t^3 + 0.001\theta^3 + 1.268t^2\theta - 0.003t\theta^2 \quad (A.4)$$

$$SEA = -0.412 + 28.180t + 0.180\theta - 21.199t^2 - 0.007\theta^2 + 0.013t\theta + 6.050t^3 + 0.095t^2\theta - 0.008t\theta^2 \quad (A.5)$$

$$F_p = -42.415 + 357.754t + 2.351\theta - 85.864t^2 - 0.081\theta^2 - 7.328t\theta + 33.688t^3 + 0.001\theta^3 + 0.980t^2\theta - 0.021t\theta^2 \quad (A.6)$$

$$SEA = -1.129 + 27.121t + 0.129\theta - 19.024t^2 - 0.003\theta^2 + 0.030t\theta + 3.872t^3 + 0.161t^2\theta - 0.011t\theta^2 \quad (A.7)$$

$$F_p = -38.624 + 324.794t + 1.980\theta - 74.964t^2 - 0.068\theta^2 - 5.988t\theta + 29.658t^3 + 0.001\theta^3 + 0.762t^2\theta - 0.038t\theta^2 \quad (A.8)$$